Research Article Vol. 12, No. 5 / 1 May 2022 / Optical Materials Express 1907
Optical Materials EXPRESS

Optical dendrites for spatio-temporal computing with few-mode fibers [Invited]

SILVIA ORTÍN,* MIGUEL C. SORIANO, INGO FISCHER, CLAUDIO R. MIRASSO, AND APOSTOLOS ARGYRIS

Instituto de Física Interdisciplinar y Sistemas Complejos (IFISC, UIB-CSIC), Campus Universitat de les Illes Balears E- 07122, Palma de Mallorca, Spain
silvia@ifisc.uib-csic.es

Abstract: Multimode fibers have been extensively used in short-range communication systems and optical imaging. More recently, they have been considered for optical computing by exploiting the complex spatial and spatio-temporal transformation at the fiber end. Mimicking the dendrites of real neurons, we consider here the spatial modes that propagate with different group velocities along the fiber as different dendritic branches. The multimode fiber plays the role of an optical dendritic unit and the signals obtained from the different dendritic branches are temporally mixed and used for spatio-temporal information processing. We numerically demonstrate the use of a few-mode, step-index fiber as a linear computing element in an ultra-fast spatio-temporal coincidence detector that operates at 40 Gb/s data encoding rate. We evaluate this detector as a linear classifier in header recognition and bit counting tasks.

1. Introduction

As a result of the increasing computing demands of our globally connected society, novel computing paradigms are on the rise [1]. A promising candidate for novel computing solutions is the so-called neuromorphic (brain-inspired) computing, which targets the goal of transferring computational mechanisms used by biological brains to hardware systems [2]. In the quest for alternative computing paradigms, unconventional physical substrates for computing are also explored [3–6]. In this context, optical systems have several advantages, in terms of operational speed, low energy consumption, and parallelism, compared to traditional electronic systems, which could be exploited for computing [7].

Optical multimode fibers (MMFs) have been used as a highly scattering medium, which scrambles the coherent light and produces random patterns that can be used for endoscopic [8] or other imaging applications [9,10]. Recently, they were proposed as hardware elements for unconventional computing [6,11–14]. In particular, MMFs came into the spotlight as a medium that can convert an input optical intensity distribution to output spatial patterns with high complexity. Depending on the geometry of the fiber, the refractive indices of the core/cladding layers, and the light wavelength used at the input, different intensity profiles of the supported spatial modes of the fiber may be obtained. At the fiber output, the overall intensity profile is the result of the linear superposition of the spatio-temporal modal electric fields. This input-to-output transformation in MMFs has been considered for optical computing functionalities, such as age prediction from images of faces and audio speech classification [6]. One can use MMFs or multimode waveguides and their input-to-output transformations as physical substrates, not only for spatial, but also for spatio-temporal information processing exploiting multidimensional speckle dynamics [13]. In this context, most of the works carried out so far focus on the combination of MMFs and artificial neural network architectures to perform computing tasks such as learning of ultrafast pulses [15], image classification [16] and identification [17], computational mode decomposition [18], or prediction fiber optics nonlinear dynamics [19]. Multi-core optical fibers [17,20] and multimode waveguide ring resonators [21]

#453506 https://doi.org/10.1364/OME.453506
Journal © 2022 Received 10 Jan 2022; revised 9 Mar 2022; accepted 11 Mar 2022; published 11 Apr 2022

Optical Materials EXPRESS

have also been suggested as an alternative physical substrate for the implementation of artificial neural networks.

The spatio-temporal properties of light propagation in MMFs share a certain analogy with the propagation of electric signals in the dendrites of biological neurons [22]. This analogy can be utilized for information processing, since dendritic computation has been identified as a major computing resource [23]. In particular, the complex morphology of the dendrites, in combination with synaptic adaptation, can be seen as a set of powerful, spatio-temporal pattern detectors [24]. Only a single dendrite has a computational power similar to that of a multi-layer perceptron [24,25].

Here, we go beyond previous works by exploiting the spatio-temporal aspects of light propagation in MMF for computing purposes. We present a numerical simulations-based proof-of-concept that exploits the computational power of a few-mode fiber (FMF) for configuring an ultra-fast spatio-temporal coincidence detector. Specifically, we make use of the different group velocities of the various fiber modes to define individual dendritic branches. Each dendritic branch is composed of all the spatial modes with the same group velocity. The temporal mixing of the different modes introduces a short-term memory of any time-encoded information. In our configuration, we consider a FMF that supports up to four dendritic branches. By introducing a mismatched alignment between the incident beam and the fiber axis of the FMF at the fiber input, we can control the number of active dendritic branches via the spatial fiber modes that are excited. This leads to different spatial intensity beam profiles at the output. The optical output is detected by single-area or segmented photodetectors (2x2 and 3x3 arrays) and is fed into a logistic regression classifier to execute computing tasks, based on coincidence detection schemes. We evaluate the classification performance of our optical dendritic unit (ODU) in two temporal tasks: a 4-bit header recognition and a "1"s counter for the 4-bit header.

2. Description of the concept

The operating principle behind the FMF-based ODU operation is shown in the geometrical representation of Fig. 1. The temporal mixing of an input signal occurs as it propagates with different group velocities, via the different spatial fiber modes. Modes with the same group velocity contribute to the same dendritic branch of the ODU. Standardized MMF at 1550nm have core diameters of 50 μm or 62.5 μm and support hundreds of spatial modes. Here, we focus on fiber designs with smaller diameter cores (FMF) that support only a small number of spatial modes. The reason for this selection is to investigate an ODU with a small number of dendritic branches and to easily decompose the contribution of each fiber mode to the spatio-temporal optical pattern obtained at the output of the fiber. However, this concept can be generalized to MMFs with large core diameters and hundreds of spatial modes.

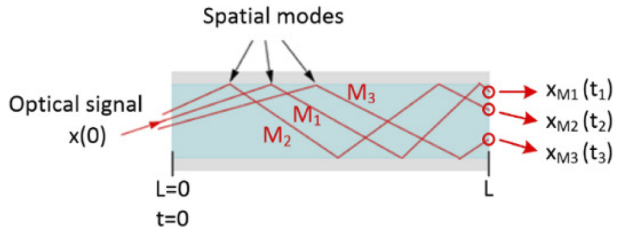

Fig. 1. A ray representation of light propagation in a MMF (FMF). An input optical signal $x(t = 0)$ may follow different paths (rays) in the propagation medium of physical length L. At the fiber end, the signal x_M arrives at different times $(t_1 - t_3)$, depending on the ray path that was followed $(M_1 - M_3)$.

Optical Materials EXPRESS

2.1. Spatio-temporal propagation and definition of the ODU

In a spatio-temporal description of pulse propagation in a MMF, along the longitudinal coordinate z and under the weakly guiding approximation, the electric field can be represented as a composition over all the modes supported by the fiber [26]:

$$E(x, y, z, t) = \mathrm{Re}[\sum_{p} \frac{\psi_p(x, y, \omega_0)}{N_p(\omega_0)} A_p(z, t) \exp^{-i\omega_0 t}] \tag{1}$$

where ω_0 is the central optical frequency, $\psi_p(x, y)$ is the spatial profile and $A_p(z, t)$ is the slowly varying complex envelope of the electric field of the p^{th} mode. The index p enumerates the LP modes in our study (Fig. 2). $N_p(\omega_0)$ is a normalization coefficient which ensures that the power of the p^{th} mode is given by $|A_p(z, t)|^2$. Each mode has a different propagation constant, $\beta^{(p)}$, which determines the phase velocity of the electric field of the p^{th} mode. In our numerical simulations we use the model of the multimode generalized nonlinear Schrödinger equation (MM-GNLSE), as presented in [27,28]. We assume linear propagation, so only the corresponding linear terms are considered. These are the terms that appear in the wave equation, derived from Maxwell's equations in a dielectric medium. The equation that gives the electric field's temporal envelope of the p^{th} spatial mode in the linear regime is:

$$\frac{\partial A_p(z, t)}{\partial z} = i\Delta\beta_0^{(p)} A_p - \Delta\beta_1^{(p)} \frac{\partial A_p}{\partial t} + \sum_{m=2}^{N_d} i^{m+1} \frac{\beta_m^{(p)}}{m!} \frac{\partial^m A_p}{\partial t^m}, \tag{2}$$

The pulse propagation is studied here using the propagation of the fundamental mode as a time reference. Consequently, the terms $\Delta\beta_0^{(p)}$ and $\Delta\beta_1^{(p)}$ express the propagation constant difference and the inverse group velocity difference with respect to the fundamental mode LP01, respectively. The third term of the equation represents higher-order dispersion effects, where we set $N_d = 4$. The terms in Eq. (2) result from approximating the frequency dependence of the propagation constant of each mode with a Taylor series around ω_0, and then applying a transformation in the time domain. We solve Eq. (2) in the spectral domain, by applying the dispersion operator to the electric field at the input of the fiber. Linear mode coupling is not considered here, as we numerically model an ideal straight-line FMF without any perturbations.

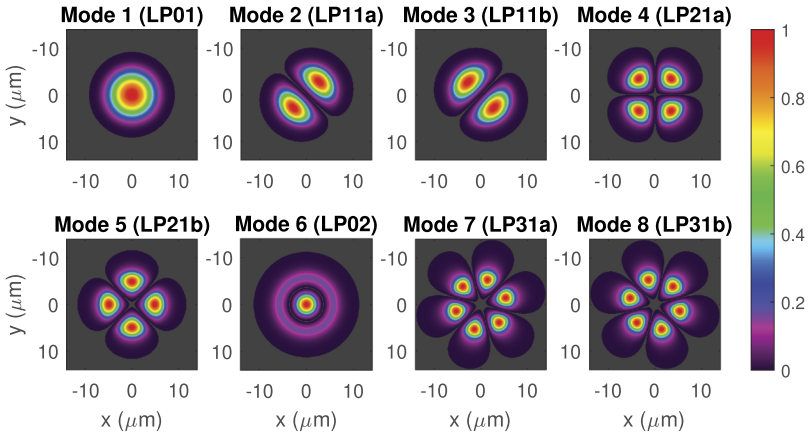

Fig. 2. Spatial normalized intensity profile of the $p = 1$ to 8 modes supported by a step-index FMF, with core diameter of 14 μm, at $\lambda_0 = 1550\ nm$.

In our FMF design, we consider silica material with a step-index profile for the core's refractive index, a refractive index difference between core and cladding of 0.0139, and a core diameter of

Optical Materials EXPRESS

14 μm. This design, at a wavelength of $\lambda_0 = 1550\,nm$, supports in total 8 modes, which correspond to five groups of LP modes: LP01, LP11, LP21, LP02, and LP31, including the degenerate mode families: LP11a/LP11b, LP21a/LP21b, and LP31a/LP31b. The linearly polarized LPj1 modes ($j \geq 1$) are two-fold degenerate, with each of the modes having different azimuthal variations of intensity, while the LP0m modes ($m \geq 1$) are instead circularly symmetric and non-degenerate. The degenerate LP modes have the same propagation constant and therefore the same group velocity. In Fig. 2, we show the corresponding spatial intensity patterns of all the supported fiber modes. Fig. 3 (left) shows the inverse group velocity of the supported fiber modes with respect to that of the fundamental LP01 mode ($p = 1$). This FMF design supports spatial modes with four different group velocities, thus defining four dendritic branches (D1-D4). Those modes that contribute to the same dendritic branch are shown with the same color in Fig. 3. The first branch (D1) is defined by the fundamental mode LP01 ($p = 1$). The second branch (D2) consists of the degenerate modes LP11a/LP11b ($p = 2$ and 3). The third branch (D3) comprises three modes, the degenerates LP21a/LP21b ($p = 4$ and 5) and the mode LP02 (p=6). Finally, the fourth branch (D4) is formed by the degenerate modes LP31a/LP31b ($p = 7$ and 8).

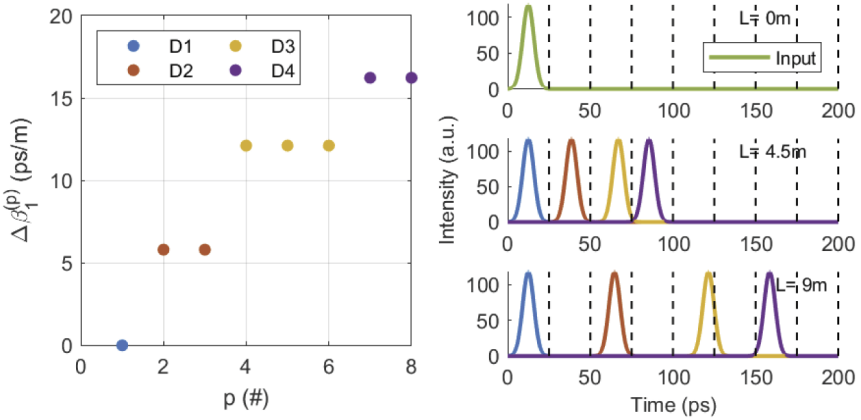

Fig. 3. Left: Inverse group velocity difference between the LP01 mode ($p = 1$) and the rest of the modes guided in the FMF. The eight different fiber modes p define four dendritic branches (different colors). Right: Temporal profile of a 25 ps Gaussian optical pulse coupled at the input of the FMF (top), after a propagation of L=4.5 m (middle), and 9 m (bottom). The four output pulses emerge after fiber propagation, due to the group velocity difference that characterizes the dendritic branches D1-D4.

In Fig. 3 (right top), we show the propagation of a 25 ps Gaussian optical pulse in the FMF at different distances. After L=4.5 m (Fig. 3 right middle), the pulse has propagated through the different modes of the fiber and the corresponding dendritic branches (shown in different colors). The emerging multiple pulses are separated in time by $\Delta\beta_1^{(p)} \cdot L$, where L is the propagation fiber length. At this length and for the chosen FMF design, the four dendritic branches result in output pulses in subsequent neighboring time frames of 25 ps each. Thus, delayed copies of the input pulse information become available in these time frames, which can be exploited as computational short-term memory. The temporal separation of the output pulses increases linearly with the fiber length. Thus, if we double the FMF length to L=9 m (Fig. 3 right bottom), the delayed copies of the information become more separated in time, although they do not cover subsequent time frames. In this case, a longer memory could be exploited.

In this study, we consider the case of a FMF with L=4.5 m, and we implement a coincidence detector using the available information in four neighboring time frames of 25 ps. In Fig. 4, we illustrate the temporal propagation of a sequence of five optical Gaussian pulses of 25 ps duration

Optical Materials EXPRESS

each. After this propagation length, the temporal distribution of one input pulse lies within a duration of 100 ps. For better understanding, we decompose the temporal output pattern that is obtained at the end of the FMF, for each of the five input pulses, in a sequence of temporal frames. Input pulse #1 results in the output frame #1, input pulse #2 results in the output frame #2, etc. In this representation, we can visually evaluate the temporal overlap between the subsequent input pulses at the output of the FMF. For example, in the time frame between 75 ps and 100 ps, the longest dendritic branch of the input pulse #1 (output frame #1, purple color) coincides with the shortest dendritic branch of the input pulse #4 (output frame #4, blue color), and also with the intermediate group velocity dendritic branches of input pulses #2 and #3 (output frames #2 – yellow color and #3 – red color, respectively). Input pulses that are separated by more than 100ps will not temporally mix at the output (e.g. pulse #1 and #5, and the corresponding output frames #1 and #5, respectively). In this case, fiber lengths longer than L=4.5 m need to be considered to extend the coincidence time window.

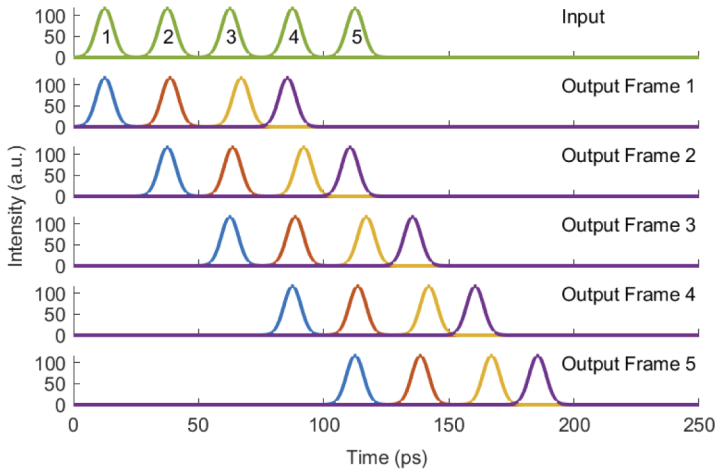

Fig. 4. Temporal sequence of five 25 ps Gaussian pulses launched sequentially at the input of the FMF (input panel). Each of the input pulses propagates along the FMF with four different group velocities, emulating equal number of dendritic branches. Input pulse #1 results in the output frame #1, etc. Within a time window of 25 ps, the information of four input pulses is mixed. The propagation length is L=4.5 m.

2.2. *Modal intensity distribution*

When an input optical beam is symmetrically coupled to the cylindrical axis of the fiber, the overlap integral of the input distribution with the fundamental fiber mode is maximized and almost the entire optical intensity propagates in the LP01 mode. Here, we aim to excite multiple propagation fiber modes with similar power. This can be achieved by misaligning the input optical beam with respect to the fiber propagation axis. The misalignment can be introduced either by transverse displacement or by angular tilt of the input beam. Although this approach results in a reduced overlap integral of the input distribution with the fundamental fiber mode, it also redistributes the optical intensity between the different modes that are supported in the fiber. In our ODU interpretation this is equivalent to activating different dendritic branches. In Fig. 5, we show three examples of light coupling at the input of the FMF and the corresponding optical power distribution to the different spatial modes. To obtain the ratio of optical power coupled into each of the supported modes, we calculate the overlap integral of the input electric field distribution of a linearly polarized Gaussian optical beam, with a waist of 12μm ($E_i(x, y)$),

Optical Materials EXPRESS

and the electric field supported by the corresponding mode ($E_p(x, y)$) [29]:

$$\eta = \frac{|\iint E_i(x,y)E_p^*(x,y)dxdy|^2}{\iint |E_i(x,y)|^2dxdy \iint |E_p(x,y)|^2dxdy} \tag{3}$$

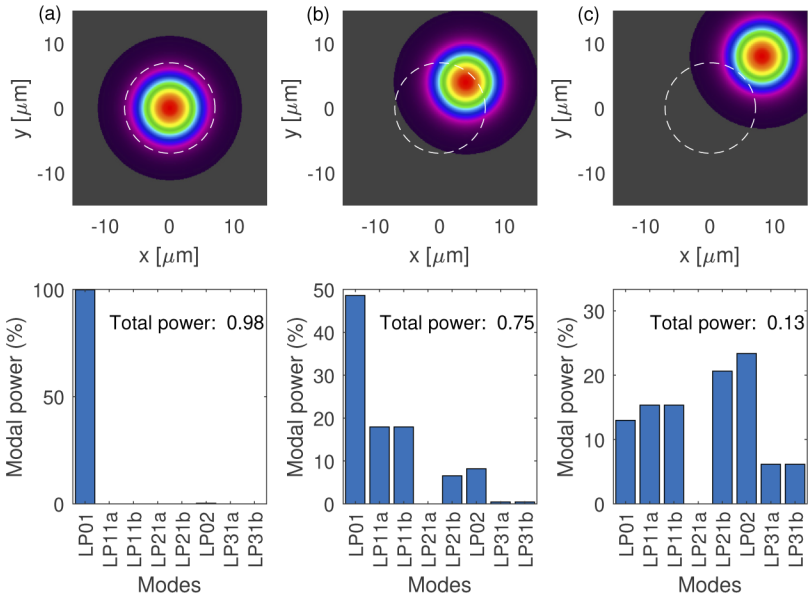

Fig. 5. Top: Transverse displacement of the optical beam coupled to the FMF core: (a) 0,0 (perfect alignment), (b) 4,4 and (c) 8,8, in μm. Bottom: Normalized optical power distribution to the FMF modes, for the corresponding three displacement conditions (a-c). The total power refers to the ratio of the optical power received at the output compared to the input. The input optical beam waist is 12 μm. The white dashed line in (a-c) indicates the position of the fiber's core.

For a perfect alignment (Fig. 5(a)), 98% of the optical power is concentrated in the LP01 mode. The remaining power is either guided in other modes or is lost through unguided, radiative modes. This solitary mode indicates the existence of only one dendritic branch (D1). When displacing the input beam by 4 μm in both transverse directions, the total optical power coupled into the fiber is reduced to 75%, but five modes are supported (Fig. 5(b)). These modes activate three dendritic branches (D1, D2, and D3), as dendritic branch D4 is associated with the two degenerate modes of LP31 that have a negligible contribution to the optical power. By further increasing the displacement of the input optical beam to 8 μm in both directions, the total optical power coupled into the fiber is further reduced to 13%. However, the number of modes that carry the optical power increase to seven and their power distribution is more balanced (Fig. 5(c)). These seven modes activate all four dendritic branches (D1-D4). As it becomes evident, the transverse displacement coupling parameter is critical to our investigations, since it determines the presence, as well as the shape and the power distribution, of the spatial profile of each dendritic branch at the output of the FMF.

3. Definition of benchmark tasks and ODU computing

In this section, we describe the operation of the proposed ODU as a linear classifier, applied on two different digital tasks, where the input is a sequence of binary digits. The concept of the ODU computing scheme is shown in Fig. 6 and is explained below. The bit "1" is represented by the

Optical Materials EXPRESS

presence of a 25 ps Gaussian optical pulse, while the bit "0" is represented by its absence. This encoding is emulated by modulating the optical beam at the input of the FMF, at a rate of 40 Gb/s, with the aforementioned Gaussian pulse. The ODU consists of the FMF segment of L=4.5 m and follows the operation shown in Fig. 4. The first benchmark task is a 4-bit header recognition, i.e. the correct classification of the 16 different possibilities of a 4-bit sequence. The target of the 4-bit header recognition task for the i^{th} input bit (b_i) is the output pattern $y_i^h = (b_{i-3}, b_{i-2}, b_{i-1}, b_i)$. The second benchmark task is a bit '1' counter of this 4-bit sequence, where for each bit b_i the target is $y_i^c = \sum_{j=i-3}^{i} b_j$.

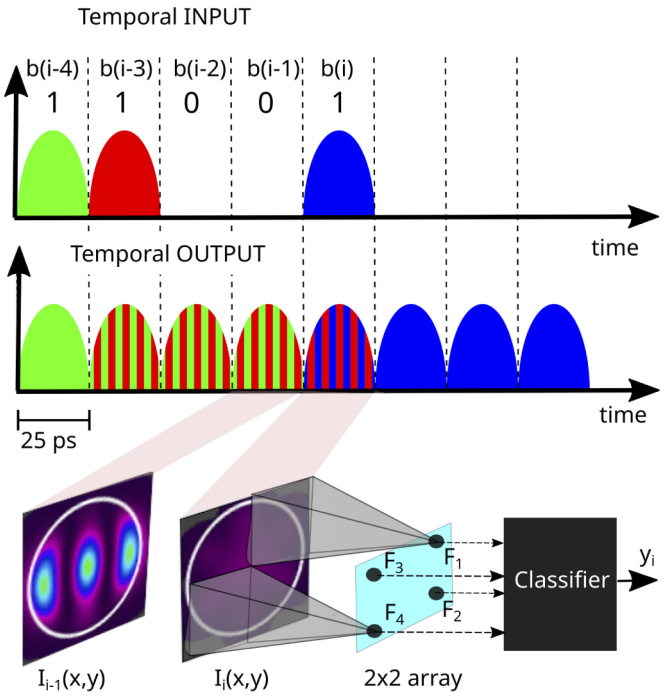

Fig. 6. Schematic of the FMF ODU computational concept. The two-colored striped pulses of the output sequence, after FMF propagation, indicate the mixing of the input information with the corresponding color. In the spatial domain, we obtain the output intensity pattern distribution $I_i(x, y)$ of each input bit b_i. Here we show photodetection of the optical intensity by a 2x2 array, which results into $n = 4$ feature values ($F_1 - F_4$) that are used by the classifier to give the corresponding output y_i.

To solve the above tasks, we first obtain the spatio-temporal intensity pattern at the output of the FMF for each i^{th} input bit, $I_i(x, y)$. This is calculated by integrating over the pulse duration (25 ps) the intensity of the electric field at the output of the FMF. For example, the spatio-temporal intensity pattern for the encoded bit #5 in Fig. 4 is equal to: $I_5(x, y) = \sum_{t=100\ ps}^{125\ ps} |E(x, y, t)|^2$. This intensity pattern, $I_5(x, y)$, contains information on only four bits, the current bit (#5) and the previous three bits (#2 to #4). Therefore, only $2^4 = 16$ possible intensity spatial profiles can be obtained at the FMF output. Fig. 7 shows these spatial intensity profiles for a transverse displacement between the optical input beam and the FMF core center of 8,8 μm. The intensity profiles were normalized in the interval [0,1], with 1 (0) corresponding to the maximum (minimum) intensity value of all 16 possible combinations.

To ensure that our numerical method is sufficiently robust, we add Gaussian white noise, with an initial signal-to-noise ratio (SNR) of 30 dB, to our system. The noise origin is associated with the spontaneous emission noise of the optical input source and the photodetection stage. We

Optical Materials EXPRESS

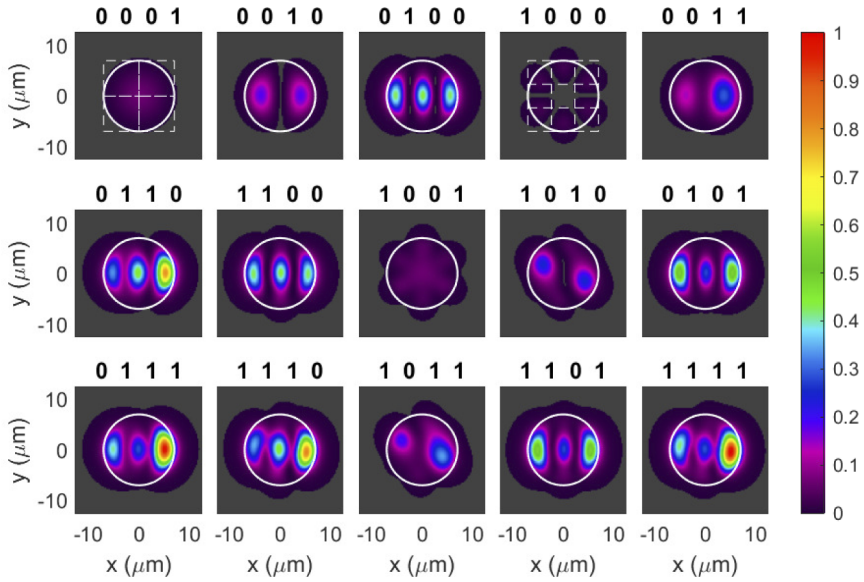

Fig. 7. Normalized spatial intensity distribution at the output of the FMF for all the 4-bit header encoding combinations $(b_{i-3}, b_{i-2}, b_{i-1}, b_i)$, except for the 0000 pattern that results in zero optical intensity. Optical input beam waist: 12 μm. The transverse displacement between the optical input beam and the FMF core center is 8,8 μm. The white line indicates the core of the fiber.

generate 103328 symbols (each symbol has 4 bits) subject to this noise, of which 3328 symbols are used in the training data set and the remaining 10^5 are used in the test set. Both data sets are class-balanced.

Depending on the photodetection approach that we adopt, n output features may be obtained from the spatial intensity profile that can be used for training the logistic regression classifier. Specifically, when we detect the entire spatial area of the output intensity profile with a single photodetection element, the overall integral is calculated, and a single value of intensity is available for training the classifier. This results in a single output feature (n=1). However, more detailed information can be obtained at the detection stage by considering segmented photodetection, i.e. a rectangular photodetection array with multiple sections. For example, a 2x2 photodetection array (Fig. 6 and Fig. 7, case 0001, dashed white frames), also known as quadrant photodetector, divides the intensity profile $I_i(x, y)$ into four non-overlapping and equal-area sections. The intensity integration is performed in each section. This approach results in n=4 output features that are now available to train the classifier and obtain the output target y_i. When considering a 3x3 photodetection array (Fig. 7, case 1000, dashed white frames) the intensity profile is divided into nine non-overlapping sections, increasing the number of output features to n=9.

The tasks described require computing systems with memory. In our case, the ODU has finite-time memory of previous states due to the different group velocities of the spatial modes. For tasks requiring memory, reservoir computing has recently become quite popular, whose – conceptually unlimited – fading memory originates from recurrent neural networks [30], dissimilar to our approach. Similar finite-time memory has been obtained by using tapped-delay neural network architectures [31]. In contrast, our FMF approach has the advantage that it does not require any delay-tapping.

Optical Materials EXPRESS

4. Results

First, we address the 4-bit header recognition task. We consider a transverse displacement condition between the optical input beam and the FMF's front facet that activates all four dendritic branches. We use the example presented in Fig. 5(c), with 8 μm displacement in x and y directions. We consider first a single photodetection unit and integrate over the overall spatial profile of the output intensity and the temporal duration of one pulse (25 ps). In this case, the spatial distribution of the intensity is not taken into account in the computation. Thus, $n = 1$ feature is used in the classifier, leading to symbol error rates (SER) above 10^{-2} in the pattern estimation of the 4-bit header, for all displacement conditions. The reason is that multiple pairs of header sequences, such as 0100,1100 or 0001,1001, result in almost the same output intensity integral. To improve the classification performance, we consider a photodetection array with a 2x2 grid distribution (Fig. 7, case 0001, dashed white frames). We consider that each panel of the array grid has a dimension of half of the fiber diameter, i.e. 7 μm x 7 μm. The overall spatial intensity profile is now segmented into four sections, and more information becomes available to the classifier's input. The corresponding integrated optical intensity in each panel of the 2x2 grid, over the 25 ps temporal window, is shown in Fig. 8. When the 4-bit header includes more "1"s, the overall power in all grids is higher. By applying the logistic regression classifier, we obtain an error-free symbol classification for the 4-bit header recognition task in the test set. Since we consider 10^5 symbols in the testing data set, error-free classification means that the error rate is below the resolution of our computation, which is 10^{-5}.

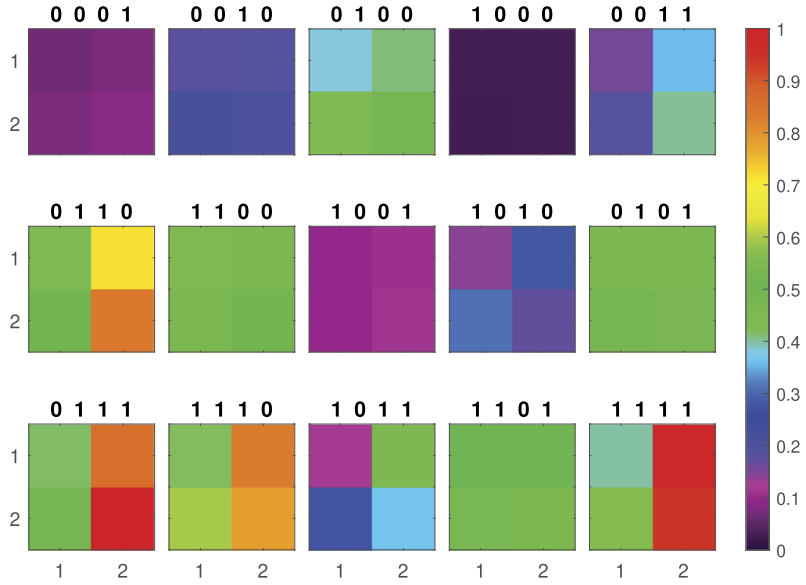

Fig. 8. Normalized optical intensity for all the 4-bit header encoding combinations, except for the 0000 pattern that results in zero optical power, obtained from the spatio-temporal patterns of Fig. 7, when integrated in four panels of the 2x2 photodetection array, over a 25 ps window.

In the previous evaluation, a specific condition for the transverse misalignment of the input coupling was considered (8 μm displacement in both x and y directions). In the following, we study the impact of different transverse displacement conditions on the classification SER of the 4-bit header recognition task. We also use the same methodology to evaluate the classification capabilities of the ODU in the counter of "1"s task. In Fig. 9, we show the classification performance for these two tasks, for different photodetection approaches, versus the coupling

Optical Materials EXPRESS

displacement between the input optical beam and the FMF in the (x, y) directions. The variation of the displacement is performed in steps of 1 μm, in both dimensions. A value of SER=10^{-5} indicates one or zero errors in the classification performance.

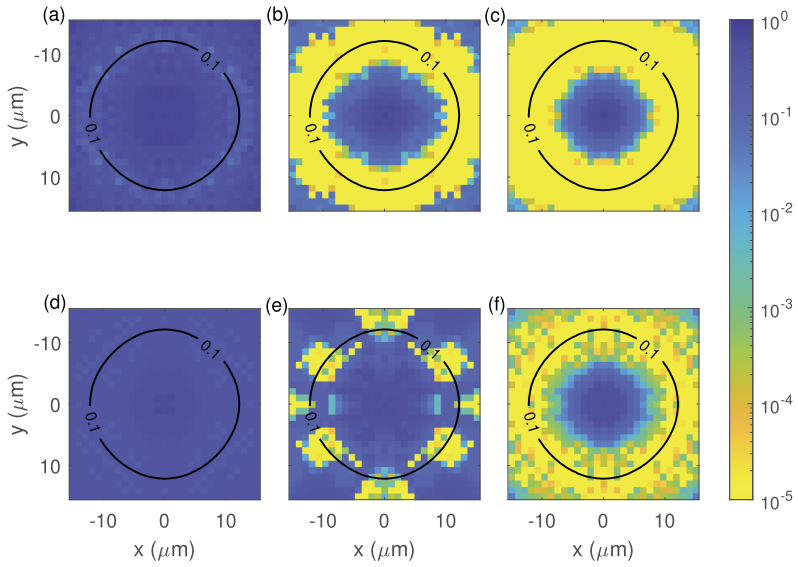

Fig. 9. Symbol error rate of the 4-bit header recognition task (a-c) and error rate of the counter of "1"s task (d-f) vs. the transverse displacement of the input optical beam with respect to the FMF core center. The optical intensity at the output is obtained via a single photodetector (a,d), a 2x2 photodetection array (b,e), and a 3x3 photodetection array (c,f). The displacement resolution step in both x and y axes is 1 μm. The contour circle line (0.1) indicates the displacement that results at the output 10% of the input optical power. Larger displacements lead to lower output power, due to higher coupling losses.

First we study the impact of the output detection approach for the 4-bit header recognition task (Fig. 9, top panels). When considering a single photodetection element (Fig. 9(a)), we do not find any displacement condition that leads to zero errors in the test dataset. When considering a 2x2 photodetection array (Fig. 9(b)), we obtain zero errors for displacements above 8 μm in both axes. We observe that, by increasing the displacement further, this performance is preserved, although it is obtained via a gradually reduced optical power. Eventually, when the detected power becomes very small, the SNR of the system degrades significantly and the system performance is affected by the photodetection noise. In contrast, when the displacement is small – as shown in Figs. 5(a) and 5(b) – some dendritic branches are not activated and the ODU does not have the required short-term memory to solve this task. As a result, the classification performance is poor. Thus, the sweet spot of best performance requires sufficient SNR and sufficient power in the different dendritic branches. In Fig. 9(c) we evaluate the SER of the 4-bit header task with the 3x3 array detection scheme. A better performance is achieved, when considering smaller input coupling displacements compared to the 2x2 grid. A displacement of at least 6 μm in both axes is now enough to obtain SER values below the 10^{-5} resolution.

In a similar way, we evaluate the error rate of the ODU for the counter of "1"s task (Fig. 9, bottom panels). When considering a single photodetection element, the classification performance is poor for all displacement conditions (Fig. 9(d)). When considering the 2x2 photodetection array (Fig. 9(e)), we find now a much narrower parameter space that provides zero errors, compared to the 4-bit header recognition task. By considering a 3x3 photodetection array (Fig. 9(f)), the classification shows zero errors for displacements of at least 7 μm in both axes.

Optical Materials EXPRESS

Finally, we evaluate the performance of these two tasks, by considering lower SNR conditions. In Fig. 10 we show the lowest error rate obtained for different values of the output SNR, for the two tasks, and for considering the 2x2 and 3x3 photodetection arrays. Each error rate value is obtained by considering ten repetitions of 10^5 test samples and is calculated as the mean value (white-filled triangles). With the error bars, we indicate the highest and lowest error among all repetitions. For the SNR cases in which no errors are found, the mean error value is indicated with color-filled triangles, at the resolution level of the computation (10^{-5}). Moreover, the error rate values correspond to those displacement conditions in the x, y axes that result in the lowest error. In all cases, the 3x3 photodetection array offers better classification, as more useful information can be processed by the classifier. The 4-bit header recognition task is easier to solve in the presence of noise, as a detected signal with SNR of 20dB is enough to result in zero classification errors. This performance is also achieved for the "1"s counter task, but only for a higher SNR.

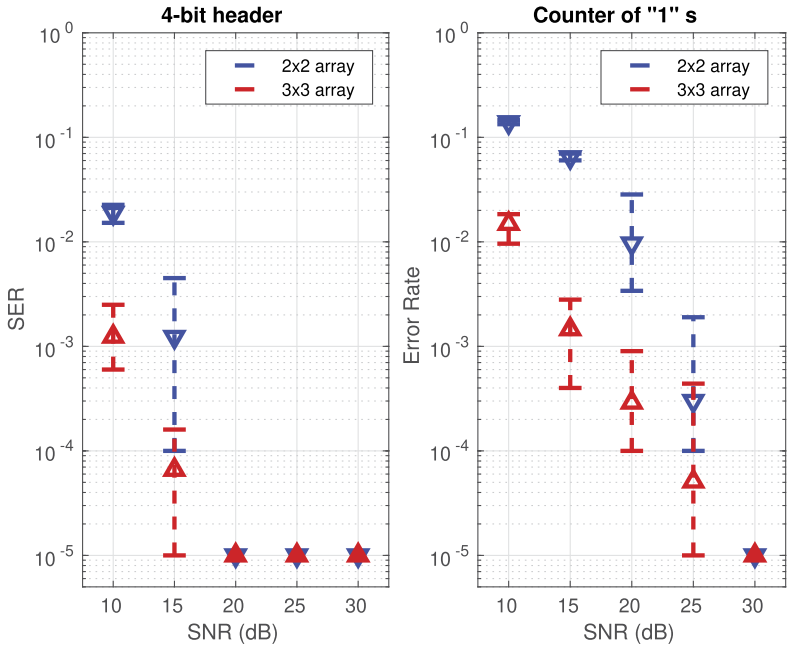

Fig. 10. Classification performance of the 4-bit header recognition and the counter of "1"s tasks vs. the SNR of the detected signals, for a 2x2 and a 3x3 photodetection array. Ten repetitions of 10^5 symbols of the testing data set were considered. The error bars indicate the maximum and the minimum error rate, among all repetitions. The white-filled triangles indicate the mean error rate of the total number of symbols. The color-filled triangles indicate that no errors are found at the resolution level of each computation (10^{-5}).

Scaling up the segmentation of the detection array allows obtaining an accurate classification with smaller input displacements, and thus higher optical power in the ODU. The compromise in this approach is using a more complex detection architecture. For more difficult tasks – e.g. header recognition with a higher number of bits – more dendritic branches in the FMF (or MMF) and an extended detection array are needed, such that the classifier accesses more information from the output spatial intensity profiles. For example, the spatio-temporal patterns could be experimentally detected via temporally resolved imaging by differential analysis [32] or via spatially resolved temporal imaging [33].

Optical Materials EXPRESS

5. Conclusions

In this work, we demonstrated a FMF as an equivalent ODU with four dendritic branches, that operates as a spatio-temporal coincidence detector. Temporal information of 40 Gb/s rate was encoded at the input and dispersed along the FMF propagation, introducing multiple delay paths with short-term memory. We showed that the spatio-temporal information at the output of a short-length FMF can be efficiently used to solve different linear computation tasks. With the appropriate fiber parametrization and length, the number of branches can be scaled up, as more modes with different modal dispersion become available. An increased number of dendritic branches and ODUs will allow the implementation of more complex tasks, such as header recognition of longer patterns.

The ODU, as introduced here, builds on the analogy with biological neurons. This analogy could be taken further by introducing nonlinearities in the optical path as suggested in [34] and, importantly, adaptation in the input-to-output optical transformation. Since adaptation (plasticity) in biological neurons often works on slower timescales than the rate of the input information [35], one could introduce optical elements such as spatial light modulators or digital micromirror devices to adapt the input-to-output spatio-temporal transformation to the desired functionality. These optical elements have been successfully employed in other optical computing approaches [6,36], showing the potential of this strategy.

Funding. Horizon 2020 Framework Programme (899265); Agencia Estatal de Investigación (PID2019-109094GB-C21, -C22/AEI /10.13039/501100011033, PID2019-111537GB-C21, MDM-2017-0711, MCIN/AEI/10.13039/501100011033).

Acknowledgments. The authors appreciate the fruitful discussions with all the scientific collaborators that participate in the H2020 FET-OPEN ADOPD project. They acknowledge the support of the European Union's Horizon 2020 research and innovation programme under grant agreement No. 899265 (ADOPD). They also acknowledge the support of the Spanish State Research Agency, through the Severo Ochoa and María de Maeztu Program for Centers and Units of Excellence in R&D , and the QUARESC and DECAPH projects.

Disclosures. The authors declare no conflicts of interest.

Data availability. Data underlying the results presented in this paper are not publicly available at this time but may be obtained from the authors upon reasonable request.

References

1. H. Jaeger, "Toward a generalized theory comprising digital, neuromorphic, and unconventional computing," Neuromorph. Comput. Eng. **1**(1), 012002 (2021).
2. C. Mead, "Neuromorphic electronic systems," Proc. IEEE **78**(10), 1629–1636 (1990).
3. M. C. Soriano, D. Brunner, M. Escalona-Morán, C. R. Mirasso, and I. Fischer, "Minimal approach to neuro-inspired information processing," Front. Comput. Neurosci. **9**, 68 (2015).
4. J. Torrejon, M. Riou, F. A. Araujo, S. Tsunegi, G. Khalsa, D. Querlioz, P. Bortolotti, V. Cros, K. Yakushiji, A. Fukushima, H. Kubota, S. Yuasa, M. D. Stiles, and J. Grollier, "Neuromorphic computing with nanoscale spintronic oscillators," Nature **547**(7664), 428–431 (2017).
5. G. Tanaka, T. Yamane, J. B. Héroux, R. Nakane, N. Kanazawa, S. Takeda, H. Numata, D. Nakano, and A. Hirose, "Recent advances in physical reservoir computing: A review," Neural Networks **115**, 100–123 (2019).
6. U. Teğin, M. Yıldırım, I. Oğuz, C. Moser, and D. Psaltis, "Scalable optical learning operator," Nat. Comput. Sci. **1**(8), 542–549 (2021).
7. H. J. Caulfield and S. Dolev, "Why future supercomputing requires optics," Nat. Photonics **4**(5), 261–263 (2010).
8. Y. Choi, C. Yoon, M. Kim, T. D. Yang, C. Fang-Yen, R. R. Dasari, K. J. Lee, and W. Choi, "Scanner-free and wide-field endoscopic imaging by using a single multimode optical fiber," Phys. Rev. Lett. **109**(20), 203901 (2012).
9. I. N. Papadopoulos, S. Farahi, C. Moser, and D. Psaltis, "Increasing the imaging capabilities of multimode fibers by exploiting the properties of highly scattering media," Opt. Lett. **38**(15), 2776–2778 (2013).
10. S. Farahi, D. Ziegler, I. N. Papadopoulos, D. Psaltis, and C. Moser, "Dynamic bending compensation while focusing through a multimode fiber," Opt. Express **21**(19), 22504–22514 (2013).
11. B. Rahmani, D. Loterie, G. Konstantinou, D. Psaltis, and C. Moser, "Multimode optical fiber transmission with a deep learning network," Light: Sci. Appl. **7**(1), 69 (2018).
12. N. Borhani, E. Kakkava, C. Moser, and D. Psaltis, "Learning to see through multimode fibers," Optica **5**(8), 960–966 (2018).
13. S. Sunada, K. Kanno, and A. Uchida, "Using multidimensional speckle dynamics for high-speed, large-scale, parallel photonic computing," Opt. Express **28**(21), 30349–30361 (2020).

Optical Materials EXPRESS

14. C. Zhu, E. A. Chan, Y. Wang, W. Peng, R. Guo, B. Zhang, C. Soci, and Y. Chong, "Image reconstruction through a multimode fiber with a simple neural network architecture," Sci. Rep. **11**(1), 896 (2021).
15. W. Xiong, B. Redding, S. Gertler, Y. Bromberg, H. D. Tagare, and H. Cao, "Deep learning of ultrafast pulses with a multimode fiber," APL Photonics **5**(9), 096106 (2020).
16. E. Kakkava, N. Borhani, B. Rahmani, U. Teğin, C. Moser, and D. Psaltis, "Deep learning-based image classification through a multimode fiber in the presence of wavelength drift," Appl. Sci. **10**(11), 3816 (2020).
17. N. Shabairou, E. Cohen, O. Wagner, D. Malka, and Z. Zalevsky, "Color image identification and reconstruction using artificial neural networks on multimode fiber images: towards an all-optical design," Opt. Lett. **43**(22), 5603–5606 (2018).
18. S. Rothe, Q. Zhang, N. Koukourakis, and J. W. Czarske, "Deep learning for computational mode decomposition in optical fibers," Appl. Sci. **10**(4), 1367 (2020).
19. U. Teğin, N. U. Dinç, C. Moser, and D. Psaltis, "Reusability report: Predicting spatiotemporal nonlinear dynamics in multimode fibre optics with a recurrent neural network," Nat. Mach. Intell. **3**(5), 387–391 (2021).
20. E. Cohen, D. Malka, A. Shemer, A. Shahmoon, Z. Zalevsky, and M. London, "Neural networks within multi-core optic fibers," Sci. Rep. **6**(1), 29080 (2016).
21. M. N. Ashner, U. Paudel, M. Luengo-Kovac, J. Pilawa, and G. C. Valley, "Photonic reservoir computer using speckle in multimode waveguide ring resonators," Opt. Express **29**(13), 19262–19277 (2021).
22. P. Poirazi and A. Papoutsi, "lluminating dendritic function with computational models," Nat. Rev. Neurosci. **21**(6), 303–321 (2020).
23. M. London and M. Häusser, "Dendritic computation," Annu. Rev. Neurosci. **28**, 503–532 (2005).
24. D. Beniaguev, I. Segev, and M. London, "Single cortical neurons as deep artificial neural networks," Neuron **109**(17), 2727–2739 (2021).
25. P. Poirazi, T. Brannon, and B. W. Mel, "Pyramidal neuron as two-layer neural network," Neuron **37**(6), 989–999 (2003).
26. C. Antonelli, M. Shtaif, and A. Mecozzi, "Modeling of nonlinear propagation in space-division multiplexed fiber-optic transmission," J. Lightwave Technol. **34**(1), 36–54 (2016).
27. L. G. Wright, Z. M. Ziegler, P. M. Lushnikov, Z. Zhu, M. A. Eftekhar, D. N. Christodoulides, and F. W. Wise, "Multimode nonlinear fiber optics: Massively parallel numerical solver, tutorial, and outlook," IEEE J. Sel. Top. Quantum Electron. **24**, 1–16 (2018).
28. F. Poletti and P. Horak, "Description of ultrashort pulse propagation in multimode optical fibers," J. Opt. Soc. Am. B **25**(10), 1645–1654 (2008).
29. M. Veettikazhy, A. K. Hansen, D. Marti, S. M. Jensen, A. L. Borre, E. R. Andresen, K. Dholakia, and P. E. Andersen, "Bpm-matlab: an open-source optical propagation simulation tool in matlab," Opt. Express **29**(8), 11819–11832 (2021).
30. M. Lukoševičius and H. Jaeger, "Reservoir computing approaches to recurrent neural network training," Comput. Sci. Rev. **3**(3), 127–149 (2009).
31. A. S. Weigend, B. A. Huberman, and D. E. Rumelhart, "Predicting the future: A connectionist approach," Int. J. Neur. Syst. **1**(3), 193–209 (1990).
32. A. Barchanski, T. Gensty, C. Degen, I. Fischer, and W. Elsasser, "Picosecond emission dynamics of vertical-cavity surface-emitting lasers: spatial, spectral, and polarization-resolved characterization," IEEE J. Quantum Electron. **39**(7), 850–858 (2003).
33. S. K. Dacha and T. E. Murphy, "Spatiotemporal characterization of nonlinear intermodal interference between selectively excited modes of a few-mode fiber," Optica **7**(12), 1796–1803 (2020).
34. M. Sorokina, "Multidimensional fiber echo state network analogue," JPhys Photonics **2**(4), 044006 (2020).
35. X.-J. Wang, Y. Liu, M. V. Sanchez-Vives, and D. A. McCormick, "Adaptation and temporal decorrelation by single neurons in the primary visual cortex," JPhys Photonics **89**(6), 3279–3293 (2003).
36. X. Porte, A. Skalli, N. Haghighi, S. Reitzenstein, J. A. Lott, and D. Brunner, "A complete, parallel and autonomous photonic neural network in a semiconductor multimode laser," JPhys Photonics **3**, 024017 (2021).